Crystal structure and magnetic properties of high-oxygen pressure annealed $Sr_{1-x}La_xCo_{0.5}Fe_{0.5}O_{3-\delta}$ ($0 \leqslant x \leqslant 0.5$)

Konrad Świerczek [a,b,1], Bogdan Dabrowski [a,b,*], Leopoldo Suescun [b,c], Stanislaw Kolesnik [a]

[a] Physics Department, Northern Illinois University, DeKalb, IL 60115, USA
[b] Materials Science Division, Argonne National Laboratory, Argonne, IL 60439, USA
[c] Cryssmat-Lab/Detema, Facultad de Química, Universidad de la República, P.O. Box 1157, Montevideo, Uruguay

ABSTRACT

Structural and magnetic studies are presented for the perovskite type $Sr_{1-x}La_xCo_{0.5}Fe_{0.5}O_{3-\delta}$ ($0 \leqslant x \leqslant 0.5$) materials annealed under moderately high-oxygen pressures of ~ 200 atm. A detailed analysis of the room temperature neutron time-of-flight diffraction data reveals that the crystal structure of the sample $SrCo_{0.5}Fe_{0.5}O_{2.89(1)}$, previously described as vacancy-disordered cubic, is similar to the formerly reported, oxygen-vacancy ordered $Sr_8Fe_8O_{23}$ compound, i.e. $Sr_8Co_4Fe_4O_{23}$ is tetragonal with the $I4/mmm$ symmetry. With an increase of the La content the studied materials become nearly oxygen stoichiometric and a lowering of the crystal symmetry is observed from cubic $Pm\bar{3}m$ ($x = 0.1$ and 0.2) to tetragonal $I4/mcm$ ($x = 0.3$ and 0.4), and finally to monoclinic $I12/c1$ ($x = 0.5$). Low-temperature structural and magnetic measurements show a ferromagnetic ordering with the maximum Curie temperature near 290 K at $x = 0.2$.

© 2008 Published by Elsevier Inc.

1. Introduction

Lanthanum strontium cobalt iron oxides with perovskite type structure have been extensively studied due to high oxygen permeability [1–7] and high mixed ionic–electronic conductivity at elevated temperatures [5,8,9], that make them attractive for applications as gas separation membranes and as the cathode materials in solid oxide fuel cells [6,7,9–11]. From the structural point of view two major phases have been obtained in the $Sr_{1-x}La_xCo_{1-y}Fe_yO_{3-\delta}$ (SLCF) system, an oxygen vacancy ordered brownmillerite type phase [12] and the cubic or pseudo-cubic perovskite phase. The brownmillerite type phase is present for materials with the oxygen vacancy concentration δ close to 0.5, and is stable in air at temperatures below 800 °C [13–16]. For samples with higher oxygen content the cubic related phases are observed in which oxygen vacancies are distributed statistically on the oxygen sublattice [15,17,18]. Also other vacancy ordered phases (e.g. $Sr_8Fe_8O_{23}$) besides the vacancy ordered brownmillerite have been observed for the Fe and Sr rich end of the SLCF series, as was reported by Hodges et al. [15]. While both oxygen stoichiometric $LaFeO_3$ and $LaCoO_3$ can easily be obtained in air,

the fully oxygenated $SrFeO_3$ requires anneal under 200 atm or higher oxygen pressure [15,19], whereas similar annealing produces oxygen deficient $SrCoO_{2.88}$ [20]. The level of the oxygen nonstoichiometry at high temperatures in the $Sr_{1-x}La_xCo_{1-y}Fe_yO_{3-\delta}$ system is determined by both, the Sr/La and Co/Fe ratios and can exceed $\delta = 0.3$. It increases with both strontium and cobalt content [5,21–24] as explained by the change of the average oxidation state of cobalt and/or iron $4-x-2\delta$ with the La^{3+}/Sr^{2+} ratio and the difficulty of obtaining Co^{4+}. This trend was observed for the mixed compositions, $SrCo_{1-x}Fe_xO_3$ prepared by high-temperature reaction [16,25] as well as by a standard ceramic method using high oxygen pressure for oxidation. Even after treating these materials under high pressure of 6 GPa in the presence of oxidizer $KClO_4$, certain oxygen deficiency was observed [26]. It was reported, however, that electrochemical oxidation allowed to obtain fully stoichiometric samples of $SrCoO_3$ [27,28] and $SrCo_{0.5}Fe_{0.5}O_3$ [29]. A recent report on stoichiometric $SrCoO_3$ obtained by a high-pressure method [30] remains to be confirmed, as the explanation for the observed excess oxygen content (>3) seems unsatisfactory. It is also worth noting that, for distorted octahedral environment and high iron content, the disproportionation reaction of Fe^{4+} to Fe^{3+} and Fe^{5+} may take place, resulting in formation of valence state 5+ of iron [31].

Previous structural reports have found a cubic perovskite structure for the oxygen deficient $SrCo_{0.8}Fe_{0.2}O_{2.78}$ [16] and for $SrCo_{0.5}Fe_{0.5}O_{2.88}$ compounds [32]. However, a number of small,

* Corresponding author at: Physics Department, Northern Illinois University, DeKalb, IL 60115, USA.

E-mail address: dabrowski@anl.gov (B. Dabrowski).

[1] Permanent address: Faculty of Materials Science and Ceramics, AGH University of Science and Technology, al. Mickiewicza 30, 30-059 Krakow, Poland.

unindexed peaks visible in the published neutron powder diffraction (NPD) patterns strongly suggest a deviation from the simple cubic perovskite structure. Also in the case of high-temperature NPD measurements performed for the $SrCo_{0.8}Fe_{0.2}O_{3-\delta}$ compound, which were fitted using the cubic $Pm\bar{3}m$ symmetry in the 873–1173 K range at $pO_2 = 1$ atm, some small, unindexed peaks are present [24].

The $Sr_{1-x}La_xCo_{1-y}Fe_yO_{3-\delta}$ system presents a vast variety of magnetic and transport properties that are strongly correlated with the chemical composition and oxygen content [33–37]. $SrFeO_3$ is metallic down to 4 K, it is antiferromagnetic with $T_N \approx 130$ K and shows a screw spin structure with $\langle 111 \rangle$ propagation vector [38,39]. It is well documented that Fe^{4+} ions present in this structure are in the high-spin (HS) state [40–43]. There is a strong hybridization present and the conduction band consists of Fe 3d and O 2p orbitals with strong negative charge transfer between iron and oxygen [42,44]. Nearly stoichiometric $SrCoO_{3-\delta}$ is also metallic and possesses ferromagnetic properties below $T_C = 222$ K [45,46] or, in case of the electrochemically oxidized sample, $T_C = 280$ K [28]. Co^{4+} cations are reported to be either in the low [28,47] or intermediate-spin (IS) state [48,49]. Negative charge transfer was also observed in this material [50]. Ferromagnetic properties were observed for mixed oxides $SrCo_{1-y}Fe_yO_{3-\delta}$ in the $0.1 \leqslant y \leqslant 0.6$ range with $T_C = 340$ K for nearly stoichiometric $SrCo_{0.6}Fe_{0.4}O_{3-\delta}$ [26]. An observation of colossal magnetoresistance at low temperatures was also reported [51,52].

Results of the magnetic and transport properties measurements for $Sr_{0.5}La_{0.5}Co_{1-y}Fe_yO_3$ $(0.0 \leqslant y \leqslant 0.6)$ indicate that the partial replacement of Co by Fe ions favors insulating and glassy magnetic behavior [37]. For the $Sr_{0.3}La_{0.7}Co_{1-y}Fe_yO_3$ $(0.0 \leqslant y \leqslant 0.6)$ series a change from ferromagnetic behavior for cobalt rich samples to antiferromagnetic G–type order for $Sr_{0.3}La_{0.7}FeO_3$ was observed. Interestingly, for the $Sr_{0.3}La_{0.7}Co_{0.5}Fe_{0.5}O_3$ composition the coexistence of ferromagnetic and antiferromagnetic domains was shown [35]. $LaCo_{0.5}Fe_{0.5}O_3$ was reported to have antiferromagnetic G–type structure below 300 K. A structural transition from $R\bar{3}c$ to low-temperature $Pbnm$ symmetry in the 200–300 K temperature range was also reported [36].

In this work we describe the structural and magnetic properties of the nearly stoichiometric system $Sr_{1-x}La_xCo_{0.5}Fe_{0.5}O_3$ $(0 \leqslant x \leqslant 0.5)$ with cubic or pseudo-cubic structures prepared by a solid state reaction technique and oxygenated under moderately high oxygen pressures.

2. Synthesis and experimental techniques

Polycrystalline $Sr_{1-x}La_xCo_{0.5}Fe_{0.5}O_{3-\delta}$ samples in the $0.0 \leqslant x \leqslant 0.5$ range were synthesized by the solid state reaction of appropriate amounts of Fe_2O_3, Co_3O_4, La_2O_3 and $SrCO_3$ (all >99.99% purity). Reactants were thoroughly mixed in an agate mortar and fired in air several times in the 900–1150 °C range with intermediate grindings. The reaction was monitored with X-ray diffraction measurements, performed after each step of the synthesis procedure using a Rigaku D/MAX powder diffractometer in the 20–70° range with Cu$K\alpha$ radiation. The final step of the synthesis procedure was an oxygenation performed under 180–200 bar of oxygen pressure at 410–500 °C followed by a very slow (0.1°/min) cooling to room temperature.

Thermogravimetric analysis (TGA) was performed on a Cahn TG171 thermobalance in several flowing gas mixtures up to 1100 °C to determine the oxygen stoichiometry as a function of oxygen pressure and temperature, and to determine the exact oxygen content of the final samples. The weight of the approximately 1 g samples was measured with a 5 μg precision. Oxygen

content in the samples was determined by the weight difference between the initial sample and total reduction products La_2O_3, SrO, and metallic Co and Fe (confirmed by X-ray powder diffraction) obtained by slow reduction in hydrogen atmosphere (1°/min) up to the point of no weight change. Fig. 1 shows exemplary TGA measurements for the $SrCo_{0.5}Fe_{0.5}O_{3-\delta}$ sample obtained from a high-pressure oxygen annealing under 200 atm at 430 °C. In the first step, the sample was heated and cooled in 0.5% O_2 in Ar, followed by a reduction in 50% H_2 in Ar. The extended equilibrium ranges of oxygen contents vs. temperature near 2.56 in 0.5% O_2/Ar and 2.50 in 50% H_2/Ar signal the presence of an oxygen vacancy ordered brownmillerite phase. Stability of such phases for various x in $Sr_{1-x}La_xCo_{0.5}Fe_{0.5}O_{3-\delta}$ their structures determined from NPD studies and properties will be described in future publications. The TGA determined oxygen contents of the high-oxygen-pressure annealed $Sr_{1-x}La_xCo_{0.5}Fe_{0.5}O_{3-\delta}$ samples were found at 2.89(1) and 2.98(1) for $x = 0$ and 0.1, respectively. The remaining samples $x = 0.2$–0.5 were found fully oxygenated to 3.00. Some of them, $x = 0.4$ and 0.5, achieved that oxygen content after slow cool in air.

Room temperature neutron time-of-flight powder diffraction data were collected for all $Sr_{1-x}La_xCo_{0.5}Fe_{0.5}O_3$ samples at the Special Environment Powder Diffractometer (SEPD) at Argonne's Intense Pulsed Neutron Source (IPNS) [53]. The high-resolution backscattering data bank ($2\theta = 144°$, Bank 1) was used for structural refinement. Low-temperature data were also collected to perform magnetic structure determination for the $Sr_{0.9}La_{0.1}Co_{0.5}Fe_{0.5}O_{2.98}$ and $Sr_{0.6}La_{0.4}Co_{0.5}Fe_{0.5}O_3$ samples. Structural refinements were performed by the Rietveld method with the GSAS/EXPGUI suite of programs [54,55]. The background was modeled using a shifted Chebyschev polynomial and the profile function was modeled using the modified Thomson–Cox–Hasting pseudo-Voigt function (TCHZ) with anisotropic broadening, convoluted with two back-to-back exponentials to model the intrinsic TOF profile shape. Absorption and extinction correction parameters were also refined. Symmetry-allowed atomic coordinates of all atoms in the unit cell were freely refined together with isotropic thermal displacement parameters for Sr/La and Fe/Co cations. In most of the cases, we were able to refine anisotropic thermal parameters of oxygen ions and the total oxygen content in the sample.
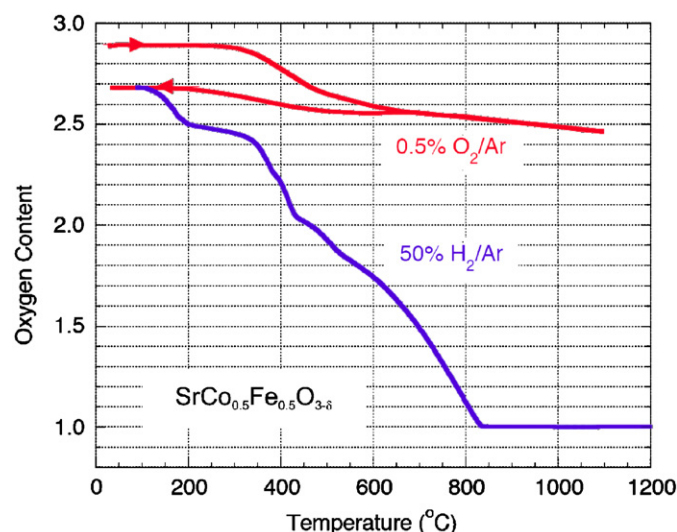

Fig. 1. Sequence of thermogravimetric measurements in 0.5% O_2/Ar (heating and cooling) and 50% H_2/Ar (heating) for the $SrCo_{0.5}Fe_{0.5}O_{3-\delta}$ sample obtained from 200 atm O_2 at 430 °C.

The dc magnetization was measured using a magnetic property measurement system model MPMS-7 (Quantum Design). The temperature dependence of magnetization was measured in the temperature range 5–395 K on cooling in a low magnetic field of 20 Oe. From that, the Curie temperature and the properties of the paramagnetic state were determined. The isothermal magnetization hysteresis loops were measured at 5 K in magnetic fields up to 70 kOe. The electrical resistivity was measured using a physical property measurement system model 6000 (Quantum Design). The temperature dependence of resistivity was measured using a standard four-point method in the temperature range 5–395 K in a zero magnetic field and in a magnetic field of 70 kOe.

3. Results and discussion

3.1. Crystal structure of the vacancy ordered $SrCo_{0.5}Fe_{0.5}O_{3-\delta}$ sample

An initial fit of the NPD data for the $SrCo_{0.5}Fe_{0.5}O_{3-\delta}$ sample was performed using cubic $Pm\bar{3}m$ symmetry. We were able to fit correctly high-intensity peaks; however a number of low-intensity peaks remained unfitted. Following the discussion presented by Hodges et al. [15] we fitted the $SrCo_{0.5}Fe_{0.5}O_{3-\delta}$ data using a tetragonal $I4/mmm$ model for the oxygen-vacancy-ordered $Sr_8Fe_8O_{23}$ compound (Fig. 2a). Apart from the improvement of the residual values of the refinement (see: footnote in Table 1), all of the previously unindexed peaks become fitted correctly (Fig. 2a). The observed vacancy ordering (Fig. 2b) has an important consequence for the interpretation of the physico-chemical properties of this material, because lower oxygen mobility can be expected as a result of such ordering; for example, it would hinder an application of such material in intermediate temperature solid oxide fuel cells (IT-SOFC), in which fast oxygen transport in the cathode material plays an important role in gaining high efficiency of a working cell. We believe that the crystal structures of the samples with similar chemical compositions showing the same low-intensity peaks and refined as cubic in [16] and [32] are indeed tetragonal $I4/mmm$ manifesting oxygen-vacancy-ordering of the $Sr_8Fe_8O_{23}$ type that appears to be quite common for the $SrCo_{1-y}Fe_yO_{3-\delta}$ compounds. It is important to note that the X-ray diffraction data of $SrCo_{0.5}Fe_{0.5}O_{3-\delta}$ show no deviation from cubic symmetry, as expected from the structural distortion arising from ordering of ~20% of oxygen vacancies, making the results of neutron diffraction of a critical importance to determine the correct structure.

Cobalt and iron cations occupy three different crystallographic sites in $Sr_8Co_4Fe_4O_{23}$, as shown in Table 1. We checked for a possibility of preferential occupation of these sites by taking advantage of the very different neutron scattering powers of Fe
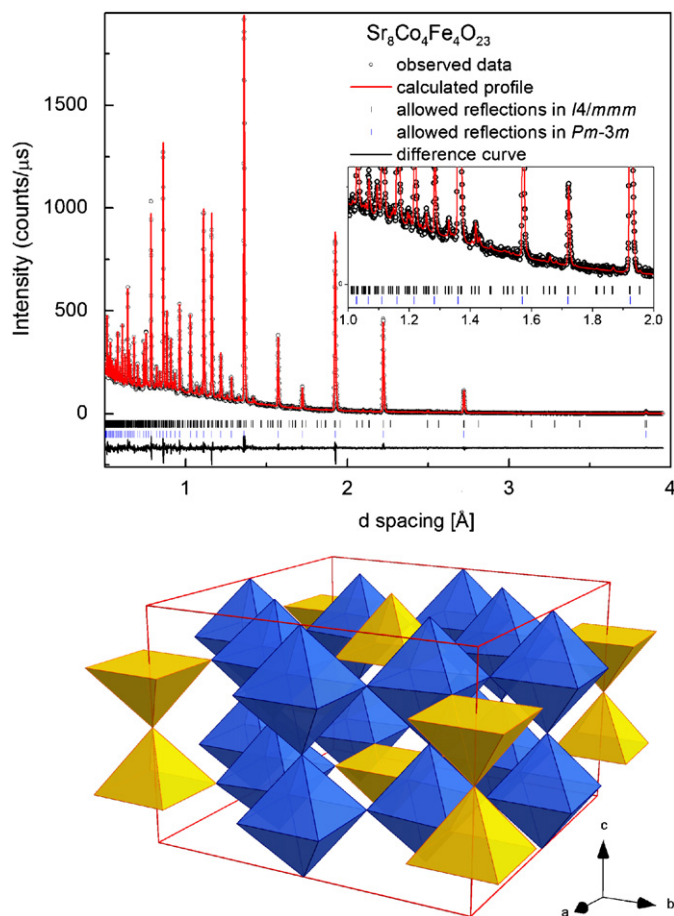

Fig. 2. (a) Room temperature NPD data and the Rietveld refinement profile using $I4/mmm$ space group for the $Sr_8Co_4Fe_4O_{23}$ sample. Top tick-marks denote allowed reflections in $I4/mmm$. Bottom tick-marks are included to emphasize the possibility of indexing the pattern using reflections in $Pm-3m$ symmetry. The inset shows a detail of the superstructure peaks in the 1–2 Å d-spacing range to emphasize that cubic model fails to describe the low-intensity peaks, which are correctly fitted by the $I4/mmm$ model. (b) Polyhedral network with ordered oxygen vacancies in $I4/mmm$ $Sr_8Co_4Fe_4O_{23}$ sample.

Table 1
Structural parameters for $Sr_8Co_4Fe_4O_{23}$ (RT).

Symmetry $I4/mmm$; $a = 10.88488(7)$ Å, $b = 10.88488(7)$ Å, $c = 7.68380(8)$ Å, $V = 910.38(2)$ Å³					
Atom	Site	x	y	z	$U_{iso} \times 100$ (Å²)
Sr(1)	8i	0.2577(2)	0	0	0.61(2)
Sr(2)	8j	0.2491(4)	0	1/2	0.88(2)
Co/Fe(1)	4e	0	0	0.2510(11)	0.44(4)
Co/Fe(2)	8f	1/4	1/4	1/4	0.62(2)
Co/Fe(3)	4d	1/2	0	1/4	0.13(3)
O(1)	2b	0	0	1/2	1.67[a]
O(2)	16m	0.1229(3)	0.1229(3)	0.2355(3)	1.51[a]
O(3)	8h	0.2460(3)	0.2460(3)	1/2	0.86[a]
O(4)	16k	0.1264(2)	0.6264(2)	1/4	1.17[a]
O(5)	4c	1/2	0	0	1.71[a]

$\chi^2 = 1.439$, $R_{wp} = 7.15\%$, and $R_p = 4.65\%$.
For comparison: $\chi^2 = 2.126$, $R_{wp} = 8.72\%$, and $R_p = 6.01\%$ when refined in cubic symmetry.
[a] U_{eqv}.

and Co (9.45 and 2.49 fm, respectively). However, no improvement of the refinement was achieved, suggesting that random distribution of the Co and Fe ions is present. We also checked for a possibility of additional nonstoichiometry in the oxygen sublattice, however also in this case no improvement of the refinement was obtained suggesting that the oxygen-vacancy ordering present in this material is complete. Selected interatomic distances and angles, shown in Table 2, are similar to the data published for $Sr_8Fe_8O_{23}$ [15]. The square–pyramidal coordinated Co/Fe(1) site exhibits slightly smaller average bond length of 1.899 Å than the octahedral Co/Fe(2) and Co/Fe(3) sites with average bonds of 1.928 and 1.937 Å, respectively. This small difference, expected as a function of coordination, as well as a small variance of the individual bond lengths does not support charge or orbital ordering on a long-range scale. The oxygen content of 2.875 (equal to 23/8) per 1 mol of the sample obtained for an ideal vacancy ordered structure is consistent with the TGA analysis which provided the oxygen content of 2.89(1).

3.2. Crystal structures of $Sr_{1-x}La_xCo_{0.5}Fe_{0.5}O_3$ $(0.1 \leqslant x \leqslant 0.5)$ samples

Contrary to the $x = 0$ sample, in case of the lanthanum substituted materials, $Sr_{1-x}La_xCo_{0.5}Fe_{0.5}O_3$ $(0.1 \leqslant x \leqslant 0.5)$, we have obtained nearly oxygen stoichiometric samples. The refined

oxygen contents from NPD data were found consistent with the TGA measurements as is shown in Tables 3–8.

$Sr_{0.9}La_{0.1}Co_{0.5}Fe_{0.5}O_{2.98}$ sample is cubic at room temperature and remains cubic down to 10 K (Table 3). The average Co/Fe–O

Table 2
Interatomic distances (Å) and bond angles (°) for the crystal structure of $Sr_8Co_4Fe_4O_{23}$ (RT).

Sr(1)–O(2)	2.687(2)	×4
Sr(1)–O(3)	2.766(3)	×2
Sr(1)–O(4)	2.678(1)	×4
Sr(1)–O(5)	2.637(3)	
Sr(2)–O(1)	2.712(4)	
Sr(2)–O(2)	2.794(3)	×4
Sr(2)–O(3)	2.678(3)	×2
Sr(2)–O(4)	2.724(2)	×4
Sr(2)–O(5)	2.731(4)	
Square–pyramidal Co/Fe(1)		
Co/Fe(1)–O(1)	1.913(9)	
Co/Fe(1)–O(2)	1.896(4)	×4
O(1)–Co/Fe(1)–O(2)	93.6(3)	×4
O(2)–Co/Fe(1)–O(2)	89.8(3)	×4
O(2)–Co/Fe(1)–O(2)	172.8(5)	×2
O(1)–O(2)	2.777(3)	×4
O(2)–O(2)	2.676(4)	×4
Octahedral Co/Fe(2) *site* ×2		
Co/Fe(2)–O(2)	1.959(4)	×2
Co/Fe(2)–O(3)	1.922(1)	×2
Co/Fe(2)–O(4)	1.903(4)	×2
O(2)–Co/Fe(2)–O(3)	91.4(2)	×2
O(2)–Co/Fe(2)–O(3)	88.6(2)	×2
O(2)–Co/Fe(2)–O(4)	90	×4
O(3)–Co/Fe(2)–O(4)	90	×4
O(2)–Co/Fe(2)–O(2)	180	
O(3)–Co/Fe(2)–O(3)	180	
O(4)–Co/Fe(2)–O(4)	180	
O(2)–O(3)	2.778(3)	×2
O(2)–O(3)	2.711(4)	×2
O(2)–O(4)	2.731(4)	×4
O(3)–O(4)	2.705(3)	×4
Octahedral Co/Fe(3) *site*		
Co/Fe(3)–O(4)	1.945(4)	×4
Co/Fe(3)–O(5)	1.921(1)	×2
O(4)–Co/Fe(3)–O(4)	90	×4
O(4)–Co/Fe(3)–O(5)	90	×8
O(4)–O(4)	2.751(4)	×4
O(4)–O(5)	2.734(2)	×8

Table 3
Structural parameters for $Sr_{0.9}La_{0.1}Co_{0.5}Fe_{0.5}O_{2.98(1)}$ as a function of temperature refined in Pm–$3m$ space group.

	10 K	100 K	200 K	RT
a (Å)	3.8262(1)	3.8272(1)	3.8313(1)	3.8397(2)
V (Å^3)	56.01(1)	56.06(1)	56.24(1)	56.61(1)
Sr/La (1a) $U_{iso} \times 100$ (Å^2)	0.33(1)	0.40(1)	0.57(2)	0.77(2)
Co/Fe (1b) $U_{iso} \times 100$ (Å^2)	0.25(1)	0.28(1)	0.37(2)	0.49(2)
O (3c) $U_{eqv} \times 100$ (Å^2)	0.64	0.69	0.87	1.11
Sr/La–O (Å) ×12	2.706(1)	2.706(1)	2.709(1)	2.715(1)
Co/Fe–O (Å) ×6	1.913(1)	1.914(1)	1.916(1)	1.920(1)
μ (μB)^a	2.58(7)	2.42(7)	1.92(8)	–
χ^2	1.388	1.376	1.321	1.445
R_{wp} (%)	7.77	7.69	7.54	5.63
R_p (%)	5.67	5.59	5.54	3.83

^{a} Refined with $P1$ magnetic symmetry for Co/Fe atoms with unit cell constrained to the nuclear phase 1a (1/2,1/2,1/2); 1b (0,0,0); and 3c (1/2,0,0).

Table 4
Structural parameters for $Sr_{0.8}La_{0.2}Co_{0.5}Fe_{0.5}O_{2.99(1)}$ refined in Pm-$3m$ space group (RT).

A (Å)	3.8410(2)
V (Å^3)	56.67(1)
Sr/La (1a) $U_{iso} \times 100$ (Å^2)	0.76(2)
Co/Fe (1b) $U_{iso} \times 100$ (Å^2)	0.44(2)
O (3c) $U_{eqv} \times 100$ (Å^2)	1.09
Sr/La–O (Å) ×12	2.716(1)
Co/Fe–O (Å) ×6	1.920(1)

$\chi^2 = 1.371$, $R_{wp} = 7.02\%$, and $R_p = 4.67\%$.

Table 5
Structural parameters for $Sr_{0.7}La_{0.3}Co_{0.5}Fe_{0.5}O_{3.00(1)}$ refined in $I4/mcm$ space group (RT).

a (Å)	5.4342(1)
c (Å)	7.6933(3)
V (Å^3)	227.19(1)
Sr/La (4b) $U_{iso} \times 100$ (Å^2)	0.80(1)
Co/Fe (4c) $U_{iso} \times 100$ (Å^2)	0.38(1)
O(1) (8h) x	0.2558(3)
O(1) $U_{eqv} \times 100$ (Å^2)	1.24
O(2) (4a) $U_{eqv} \times 100$ (Å^2)	0.90
Sr/La–O(1) (Å) ×4	2.750(2)
Sr/La–O(1) (Å) ×4	2.687(2)
Sr/La–O(2) (Å) ×4	2.717(1)
Co/Fe–O(1) (Å) ×4	1.922(1)
Co/Fe–O(2) (Å) ×2	1.923(1)
Co/Fe–O(1)–Co/Fe (°) ×2	177.3(2)
Co/Fe–O(2)–Co/Fe (°)	180
$\langle$Sr/La–O$\rangle_g$ (Å)	2.718
$\langle$Co/Fe–O$\rangle_g$ (Å)	1.922
$\langle$Co/Fe–O–Co/Fe$\rangle_g$ (°)	178.2
t_g	1.000

$\chi^2 = 1.381$, $R_{wp} = 5.69\%$, and $R_p = 3.80\%$.
4b (0,1/2,1.4), 4c (0,0,0), 8h (x,x+1/2,0),4a (0,0,1/4).

Table 6
Structural parameters for $Sr_{0.6}La_{0.4}Co_{0.5}Fe_{0.5}O_{3.00(1)}$ refined in $I4/mcm$ space group (RT) (oxygen content taken from TG data).

a (Å)	5.4378(1)
c (Å)	7.6983(3)
V (Å³)	227.64(1)
Sr/La (4b) $U_{iso} \times 100$ (Å²)	0.89(2)
Co/Fe (4c) $U_{iso} \times 100$ (Å²)	0.35(2)
O(1) (8h) x	0.2583(3)
O(1) $U_{eqv} \times 100$ (Å²)	1.39
O(2) (4a) $U_{eqv} \times 100$ (Å²)	1.08
Sr/La–O(1) (Å) ×4	2.766(2)
Sr/La–O(1) (Å) ×4	2.675(2)
Sr/La–O(2) (Å) ×4	2.719(1)
Co/Fe–O(1) (Å) ×4	1.924(1)
Co/Fe–O(2) (Å) ×2	1.925(1)
Co/Fe–O(1)–Co/Fe (°) ×2	176.2(2)
Co/Fe–O(2)–Co/Fe (°)	180
$\langle$Sr/La–O$\rangle_g$ (Å)	2.720
$\langle$Co/Fe–O$\rangle_g$ (Å)	1.924
$\langle$Co/Fe–O–Co/Fe$\rangle_g$ (°)	177.5
t_g	0.9997

$\chi^2 = 1.437$, $R_{wp} = 6.73\%$, $R_p = 4.40\%$.

Table 7
Structural parameters for $Sr_{0.6}La_{0.4}Co_{0.5}Fe_{0.5}O_{3.00(1)}$ as a function of temperature refined in $Ibam$ space group.

	10 K	100 K	200 K
a (Å)	5.4195(3)	5.4220(2)	5.4290(2)
b (Å)	5.4318(3)	5.4325(3)	5.4377(2)
c (Å)	7.6630(4)	7.6654(3)	7.6737(3)
V (Å³)	225.58(3)	225.79(1)	226.54(1)
Sr/La (4b) $U_{iso} \times 100$ (Å²)	0.39(2)	0.47(2)	0.63(2)
Co/Fe (4c) $U_{iso} \times 100$ (Å²)	0.12(2)	0.15(2)	0.17(2)
O(1) (8j) x	0.2595(9)	0.2593(9)	0.2589(9)
O(1) y	0.2355(7)	0.2361(7)	0.2379(7)
O(1) $U_{iso} \times 100$ (Å²)	0.69(4)	0.76(4)	0.76(3)
O(2) (4a) $U_{iso} \times 100$ (Å²)	0.67(8)	0.62(7)	1.10(7)
Sr/La–O(1) (Å) ×4	2.777(2)	2.776(2)	2.773(2)
Sr/La–O(1) (Å) ×4	2.647(2)	2.650(2)	2.658(2)
Sr/La–O(2) (Å) ×2	2.716(1)	2.716(1)	2.719(1)
Sr/La–O(2) (Å) ×2	2.710(1)	2.711(1)	2.715(1)
Co/Fe–O(1) (Å) ×2	1.901(5)	1.903(6)	1.910(6)
Co/Fe–O(1) (Å) ×2	1.940(6)	1.939(6)	1.935(6)
Co/Fe–O(2) (Å) ×2	1.916(1)	1.916(1)	1.918(1)
Co/Fe–O(1)–Co/Fe (°) ×2	174.5(1)	174.7(1)	175.2(1)
Co/Fe–O(2)–Co/Fe (°)	180	180	180
$\langle$Sr/La–O$\rangle_g$ (Å)	2.712	2.713	2.716
$\langle$Co/Fe–O$\rangle_g$ (Å)	1.919	1.919	1.921
$\langle$Co/Fe–O–Co/Fe$\rangle_g$ (°)	176.3	176.4	176.8
t_g	0.9993	0.9997	0.9997
μ_z (μB)	2.66(7)	2.32(7)	–
χ^2	1.451	1.361	1.386
R_{wp} (%)	7.36	7.04	7.07
R_p (%)	5.43	5.18	5.19

4b (1/2,0,1/4), 4c (0,0,0), 8j (x,y,0), 4a (0,0,1/4).

Table 8
Structural parameters for $Sr_{0.5}La_{0.5}Co_{0.5}Fe_{0.5}O_{3.02(1)}$ refined in $I12/c1$ space group (RT).

a (Å)	5.4427(1)
b (Å)	5.4523(1)
c (Å)	7.7119(2)
β (°)	90.256(1)
V (Å³)	228.85(1)
Sr/La (4e) y	0.5004(10)
Sr/La $U_{iso} \times 100$ (Å²)	0.80(1)
Co/Fe (4a) $U_{iso} \times 100$ (Å²)	0.49(1)
O(1) (8f) x	0.2659(5)
O(1) y	0.2382(7)
O(1) z	−0.0129(3)
O(2) (4e) y	0.0218(7)
O(1) $U_{eqv} \times 100$ (Å²)	1.29
O(2) $U_{eqv} \times 100$ (Å²)	1.19
Sr/La–O(1) (Å) ×2	2.877(3)
Sr/La–O(1) (Å) ×2	2.729(5)
Sr/La–O(1) (Å) ×2	2.582(3)
Sr/La–O(1) (Å) ×2	2.721(4)
Sr/La–O(2) (Å)	2.610(5)
Sr/La–O(2) (Å)	2.843(5)
Sr/La–O(2) (Å) ×2	2.724(1)
Co/Fe–O(1) (Å) ×2	1.947(4)
Co/Fe–O(1) (Å) ×2	1.916(4)
Co/Fe–O(2) (Å) ×2	1.932(1)
Co/Fe–O(1)–Co/Fe (°) ×2	171.3(1)
Co/Fe–O(2)–Co/Fe (°)	173.0(2)
$\langle$Sr/La–O$\rangle_g$	2.725
$\langle$Co/Fe–O$\rangle_g$	1.932
$\langle$Co/Fe–O–Co/Fe$\rangle_g$ (°)	171.9
t_g	0.9973

$\chi^2 = 1.636$, $R_{wp} = 4.41\%$, $R_p = 2.95\%$.
4e (1/4,y,0), 4a (0,0,0), 8f (x,y,z).

would expect an observation of the signs of symmetry lowering in the diffraction data. However, within the resolution of our NPD data we could not observe this effect. Therefore, to refine magnetic moment we included a second phase for the NPD data fitting, with the unit cell and Co/Fe positions constrained to the nuclear cubic cell, and modeling only the magnetic contribution to the data. The refined magnetic moment at 10 K was found to be equal to 2.58(7) μB and agreed well with the magnetization data presented in Section 3. Because we could not observe the symmetry breaking, we assumed an arbitrary direction of the magnetic moment. The observed increase of the magnetic moment and decreases of the lattice parameter, bond lengths and thermal parameters with decreasing temperature are typical for the ferromagnetic oxide system (Table 3).

Similarly to the above composition, the $Sr_{0.8}La_{0.2}Co_{0.5}Fe_{0.5}O_3$ sample is cubic at RT and has minimally larger unit cell (Table 4) as expected from the increase of the La^{3+} content. However, within an error bar we did not observe the corresponding elongation of the Co/Fe–O bond length that was expected for a slightly reduced average oxidation state of $4-x-2\delta = 3.8$ as compared with 3.86 for the $Sr_{0.9}La_{0.1}Co_{0.5}Fe_{0.5}O_{2.98}$ sample. The variable charge and spin state of Co, which affects its ionic size may be a reason for that.

The room temperature NPD data for $Sr_{0.7}La_{0.3}Co_{0.5}Fe_{0.5}O_3$ material could not be fitted with the cubic structure as additional peaks were also observed, suggesting the presence of lower symmetry phase. A relatively good fit was obtained using trigonal $R\bar{3}c$ symmetry for the main phase; however, the best fit was obtained using the tetragonal $I4/mcm$ space group (see Table 5). The secondary phase was identified as a perovskite type phase with $R\bar{3}c$ symmetry. The weight percentage of this phase was refined at 4.0(5) %. In $I4/mcm$ symmetry the dodecahedral coordination sphere of Sr/La ions have three different sets of four

bond length of 1.920(1) Å reflects probably combination of various ionic sizes of Co and Fe at several valences and spin states. There is no evidence for any kind of ordering on the Sr/La or Co/Fe sublattices. In accordance with the magnetic data presented in the following section, the $Sr_{0.9}La_{0.1}Co_{0.5}Fe_{0.5}O_{2.98}$ compound is ferromagnetic below room temperature. As the onset of the ferromagnetic ordering should break cubic symmetry of the system one

identical Sr/La–O distances. Octahedral coordination of Co/Fe cations is split into two sets of four and two identical Co/Fe–O distances. The resulting average Co/Fe–O bond increases slightly to 1.922(1) Å in line with reduced average valence of 3.7. Tolerance factor t calculated using geometrical averages of bond distances [56] is within experimental error equal to 1.0000. In $I4/mcm$ symmetry the Co/Fe–O octahedron is rotated along the c-axis, with the resulting planar Co/Fe–O–Co/Fe bond angle of 177.3°, exhibiting just slight deviation from a straight bond. Both the tolerance factor and the average Co/Fe–O–Co/Fe bond angle (178.2°) show that the tetragonal distortion is very small at room temperature.

Refined structural parameters of the room temperature NPD data for $Sr_{0.6}La_{0.4}Co_{0.5}Fe_{0.5}O_3$ sample performed in tetragonal symmetry are presented in Table 6. Apart from the main phase ($I4/mcm$), the secondary phase with $R\bar{3}c$ symmetry was also observed (7.5(5) wt%). Probably due to the higher amount of the secondary phase showing large degree of peak overlap with the main one, we were not able to reliably refine the oxygen content of the former, thus, the total oxygen content was fixed to 3.00 as suggested by the TGA data (3.00(1)). Further increase of the tetragonal distortion was observed as exhibited by an increase of the average Co/Fe–O bond length to 1.924(1) Å and a deviation from a straight planar Co/Fe–O–Co/Fe bond angle to 176.2° in line with the reduced average valence to 3.6.

For the $Sr_{0.6}La_{0.4}Co_{0.5}Fe_{0.5}O_3$ sample low-temperature NPD data were also collected. Results of refinements are shown in Table 7. At 200 K tetragonal symmetry was no longer giving good fit to the data. However, the use of the orthorhombic $Ibam$ space group resulted in a satisfactory fit. In this symmetry a further separation of atomic distances is present: distances in dodecahedral coordination of Sr/La ions are split into four groups, while in case of the $(Co/Fe)O_6$ octahedra three different interatomic distances are present. While the azimuthal Co/Fe–O–Co/Fe bond angle remains at 180°, two angles in the equatorial plane are equal to 175.2°. A refinement of similar quality was obtained for the $Pnma$ space group. However, a large number of anticipated reflections, which were not present in the data, strongly support the use of the higher symmetry $Ibam$ space group. The magnetization data presented in the following chapter revealed ferromagnetic properties of this material below 185 K. The NPD data refinement for 100 and 10 K is in a good agreement with the magnetization data, the refined magnetic moments are 2.32(7) and 2.66(7), respectively, and the moments are directed along the crystallographic c-axis. It is worth pointing out that the structural transition from the high-temperature tetragonal to the low-temperature orthorhombic structure, which takes place between 300 and 200 K, is independent of the paramagnetic–ferromagnetic transition. Typical temperature trends of decreasing cell and thermal parameters (refined isotropically) and an increased orthorhombic distortion as measured by the decreasing tolerance factor and the average Co/Fe–O–Co/Fe bond angle were observed (see Table 7).

In the case of the $Sr_{0.5}La_{0.5}Co_{0.5}Fe_{0.5}O_3$ composition it was not necessary to use elevated oxygen pressure to obtain oxygen stoichiometric sample. The TGA measurements for the sample heated and slowly cooled from 1150 °C in air revealed the perfect 3.00(1) stoichiometry. The room temperature NPD data for this material could not be satisfactorily fitted in either tetragonal or orthorhombic symmetry. However, by using monoclinic $I12/c1$ space group we were able to obtain a very good fit ($\chi^2 = 1.636$, $R_{wp} = 4.41\%$, $R_p = 2.95\%$) in comparison to the fit in which orthorhombic space group was used ($\chi^2 = 4.892$, $R_{wp} = 7.63\%$, $R_p = 5.15\%$). Fig. 3 shows the NPD data and Rietveld refinement and the structural results are presented in Table 8. In the $I12/c1$ space group, multiple Sr/La–O and three different Co/Fe–O atomic
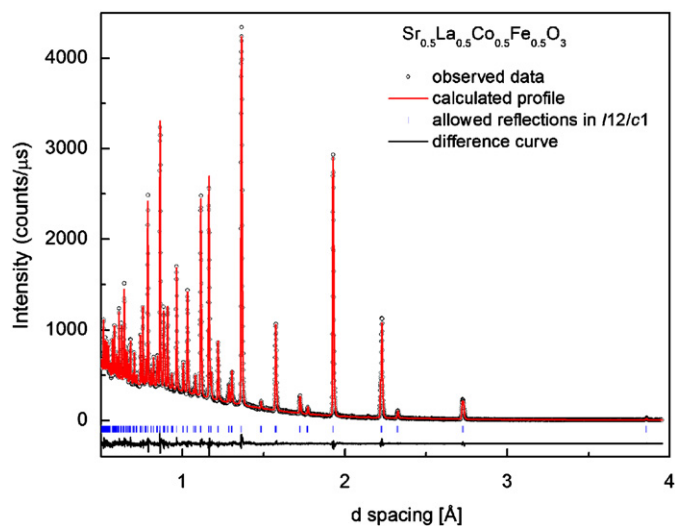

Fig. 3. Room temperature NPD data and the Rietveld refinement profile in $I12/c1$ space group for $Sr_{0.5}La_{0.5}Co_{0.5}Fe_{0.5}O_3$ sample.

distances are present. The major difference with respect to the tetragonal $I4/mcm$ and orthorhombic $Ibam$ symmetry observed for the $x = 0.3$ and 0.4 samples is the appearance of the Co/Fe–O octahedral tilting along the a and b axes in addition to the c-axis rotation, resulting in the apical and equatorial Co/Fe–O–Co/Fe bond angles of 173.0° and 171.3°, respectively. Comparing the structural parameters for this composition with previous samples one may observe further rapid distortion of the structure (the lower tolerance factor of 0.9973 and the average bond angle Co/Fe–O–Co/Fe of 171.9°). The oxygen content of 3.02(1) refined from neutron diffraction data is in agreement with TGA data within experimental error.

The summary of observed average bond lengths Sr/La–O and Co/Fe–O, normalized cell parameters, the tolerance factor, and the normalized cubic volume are presented in Fig. 4 as a function of the chemical composition $x = 0.1$–0.5. The nonlinear dependence of all the parameters is observed, with a larger distortion from the ideal cubic structure developing for the higher lanthanum content. This may be associated with the fact that substitution of smaller strontium with larger lanthanum cations is compensated by even faster increase of the size of Co/Fe caused by nonlinear decrease of the oxidation state of Co and Fe as well as a possible increase of the Co spin state. Furthermore, an increase of the electrical resistivity (see: next section) that is also observed as a result of the substitution suggests the localization of electrons, which may also increase the average Co/Fe–O bond length through the loss of the electron kinetic energy.

The observed lowering of the symmetry in the $Sr_{1-x}La_xCo_{0.5}Fe_{0.5}O_3$ series indicates that the size of the B-site ion increases faster than that of the A-site ion, promoting BO_6 octahedral tilting that disturbs the perfect A-site coordination and decreases calculated average A–O bond distances. Starting from the cubic $a^0a^0a^0$ tilt mode (using Glazer notation [57]) an initial antiphase rotation along the c-axis is observed to yield $a^0a^0c^-$ system in the $I4/mcm$ space group of $Sr_{0.7}La_{0.3}Co_{0.5}Fe_{0.5}O_3$. The orthorhombic $Ibam$ structure found at low temperatures for the $Sr_{0.6}La_{0.4}Co_{0.5}Fe_{0.5}O_3$ sample shows the same kind of tilting as the tetragonal $I4/mcm$ structure. The symmetry loss appears from the differentiation of Co/Fe–O equatorial bond distances that breaks the four-fold symmetry of the Co/Fe site. An increasing splitting with decreasing temperature is observed, indicating that the transition from the tetragonal to orthorhombic phase on cooling is not related to the change in the tilt mode. The degree of
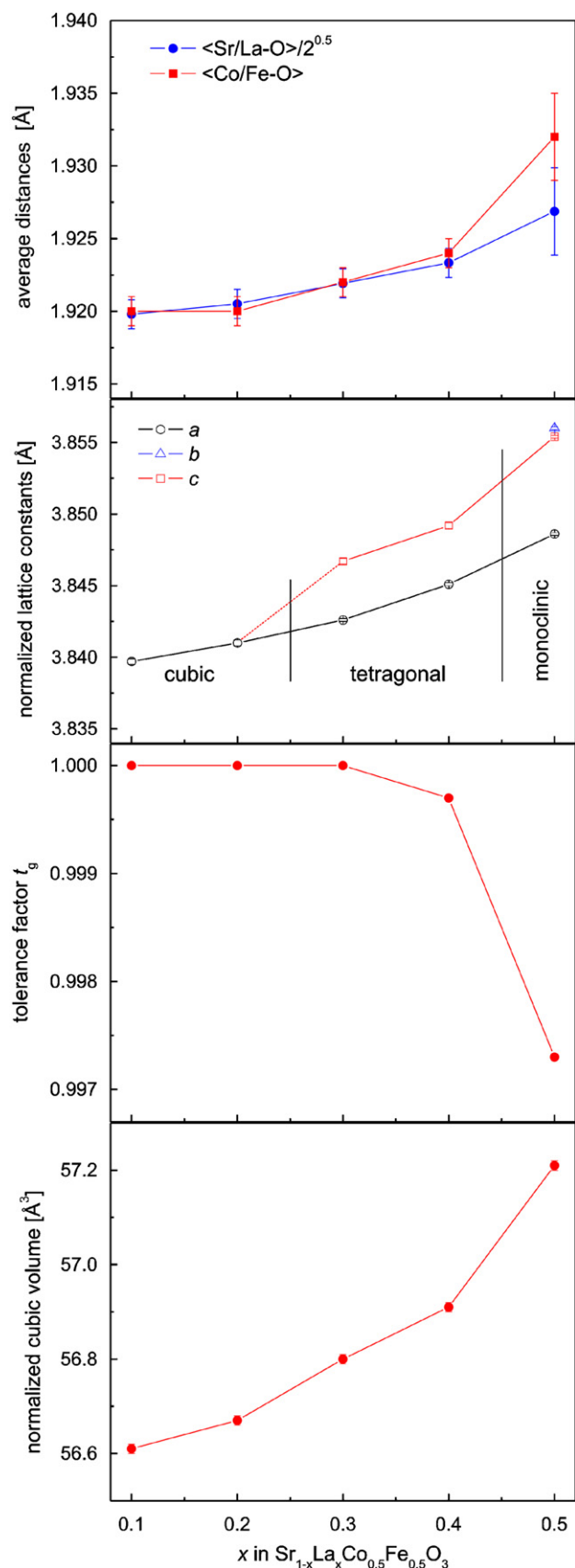
Fig. 4. Variation of: (a) average Sr/La–O and Co/Fe–O bond distances, (b) lattice parameters compared to cubic lattice constant, (c) tolerance factor t_g (calculated using geometrical average, Ref. [56]), and (d) normalized cubic volume of the perovskite unit cell at RT as a function of chemical composition x.

tilting in the orthorhombic, low-temperature structures, however, is still larger than the one observed in the room temperature tetragonal one. The monoclinic $I12/c1$ structures show not only antiphase octahedral tilting along the c-axis but also along the other two cubic directions with similar magnitudes, defining the $a^-a^-c^-$ tilt mode (or $a^-b^-b^-$ in the axes chosen by Glazer), but also significant octahedral distortion indicating again the existence of multiple structural distortions causing the symmetry reduction. The three $I4/mcm$, $Ibam$ and $I12/c1$ space groups do not share group-subgroup relations, confirming that the symmetry loss cannot be correlated with the continuous variation of one structural feature in the system.

4. Magnetic and transport properties of $Sr_8Co_4Fe_4O_{23}$ and $Sr_{1-x}La_xCo_{0.5}Fe_{0.5}O_3$ samples

A typical magnetic behavior of $Sr_{1-x}La_xCo_{0.5}Fe_{0.5}O_3$ is presented in Fig. 5. The measured materials $x = 0$–0.3 demonstrate ferromagnetic transitions at temperatures (T_C) close to or below room temperature. At $T = 5$ K, magnetic hysteresis can be observed with coercivity fields 200–2000 Oe, increasing with the La substitution. The analysis of M_{sat} requires to consider (without an additional cation disproportionation) four magnetic ions Co^{4+}, Co^{3+}, Fe^{4+}, and Fe^{3+} in different proportions depending on x. Assuming uniform reduction of Fe and Co on the increase of x, the respective cation concentrations are equal to $0.5(1-x-2\delta)$ for $(Co,Fe)^{4+}$ and $0.5(x+2\delta)$ for $(Co,Fe)^{3+}$ (for a given oxygen deficiency δ). Therefore, M_{sat} can be expressed as a function of the spin of each ion by the formula $M_{sat} = (1-x-2\delta)S_{Co4+}+(1-x-2\delta)S_{Fe4+}+(x+2\delta)S_{Co3+}+(x+2\delta)S_{Fe3+}$. If we considered all magnetic ions in the HS state, then $S_{Co4+}(HS:t_{2g}^3e_g^2) = 5/2$, $S_{Co3+}(HS:t_{2g}^4e_g^2) = 2$, $S_{Fe4+}(HS:t_{2g}^3e_g^1) = 2$, $S_{Fe3+}(HS:t_{2g}^3e_g^2) = 5/2$. In this model, if all the magnetic ions are involved in the ferromagnetic exchange, M_{sat} is constant and equal to 4.5, independent of x and δ. This model is not consistent with our results. Moreover, the HS state for Co^{4+} is less likely than the IS state $[S_{Co4+}(IS:t_{2g}^4e_g^1) = 3/2]$ in perovskite cobaltites [30] and other spin states for Co^{4+} and Co^{3+} should be considered. To simplify the analysis, we take into account the observation of the G-type antiferromagnetism with a small spontaneous magnetization $\sim 0.1\,\mu_B$ in $LaCo_{0.5}^{3+}Fe_{0.5}^{3+}O_3$ [36]. Therefore, we assume that $(Co,Fe)^{3+}$ ions do not contribute to M_{sat} and only $(Co,Fe)^{4+}$ participate in the ferromagnetic superexchange. Together with the the IS state for Co^{4+} and the oxygen deficiency from NPD ($\delta = 0.125$ for $Sr_8Co_4Fe_4O_{23}$, $\delta = 0.02$ for
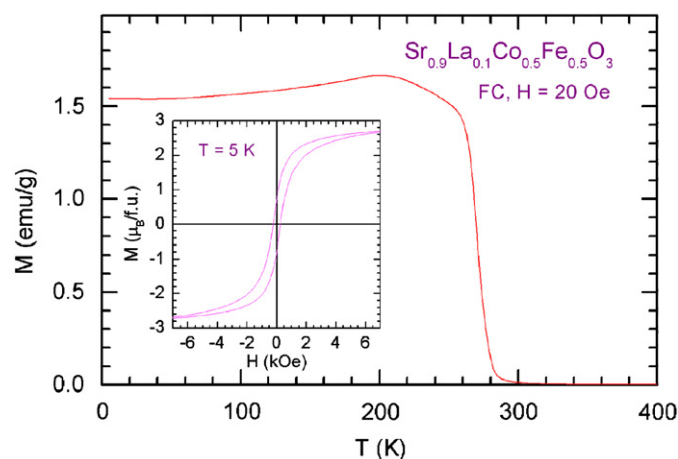

Fig. 5. Temperature dependence of magnetization for $Sr_{0.9}La_{0.1}Co_{0.5}Fe_{0.5}O_{3-\delta}$ measured on "field cooling" (FC) in a magnetic field of 20 Oe. Inset: magnetic hysteresis loop at $T = 5$ K.

$x = 0.1$, and $\delta = 0.01$ for $x = 0.2$), the latter model gives us the dependence of $M_{sat} = (1-x-2\delta)(S_{Co4+}+S_{Fe4+}) = 3.5(1-x-2\delta)$, which is presented in Fig. 6. This dependence can reproduce the experimental data pretty well.

The molar magnetic susceptibility, $\chi_m = M/H$, in the paramagnetic region above T_C, was used to determine the effective paramagnetic moment μ_{eff}, by fitting the Curie–Weiss formula $\chi_m = \chi_0 + (1/8) * \mu_{eff}^2/(T - \Theta)$. In this formula χ_0 is a temperature-independent susceptibility, $\mu_{eff} = g\sqrt{S(S + 1)}$ is the spin-only effective paramagnetic moment ($g = 2$ is the gyromagnetic factor and S is the effective spin) and Θ is the paramagnetic Curie–Weiss temperature. The values of μ_{eff} and Θ are also presented in Fig. 6.

The resultant μ_{eff} can be expressed by the spin of each magnetic ion as $\mu_{eff}^2 = 2[(1-x-2\delta)S_{Co4+}(S_{Co4+}+1)+(1-x-2\delta)S_{Fe4+}(S_{Fe4+}+1)+(x+2\delta)S_{Co3+}(S_{Co3+}+1)+(x+2\delta)S_{Fe3+}(S_{Fe3+}+1)]$. The upper limit for μ_{eff} can be reached for all magnetic ions in the HS state. That gives a constant value $\mu_{eff} = 5.43$ for each x and δ [the line for Co^{4+}:HS+Co^{3+}:HS in Fig. 6(a)]. The more realistic choice of IS states for both Co^{4+} and Co^{3+} [S_{Co4+}(IS:$t_{2g}^4 e_g^1$) = 3/2, S_{Co3+}(IS:$t_{2g}^5 e_g^1$) = 1] gives lower μ_{eff} [the line for Co^{4+}:IS+Co^{3+}:IS in Fig. 6(a)]. The observed large values of μ_{eff} may be related to the presence of ferromagnetic clusters in the vicinity of T_C. The determined values of μ_{eff} are only approximate because of using a small fitting range 350–395 K that is not much higher than the Curie temperatures. At these temperatures, the Curie–Weiss formula may not be strictly valid. The paramagnetic Curie–Weiss temperature Θ is positive as expected for ferromagnetic materials and follows closely T_C for most compositions. The reason for the larger differences between T_C and Θ for larger x is unknown. All the parameters presented in Fig. 6 demonstrate a maximum
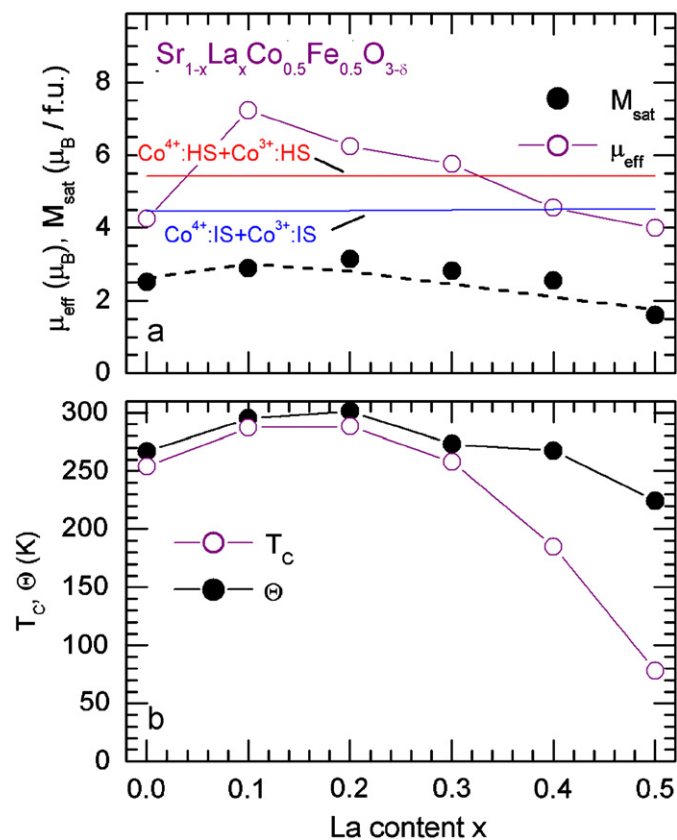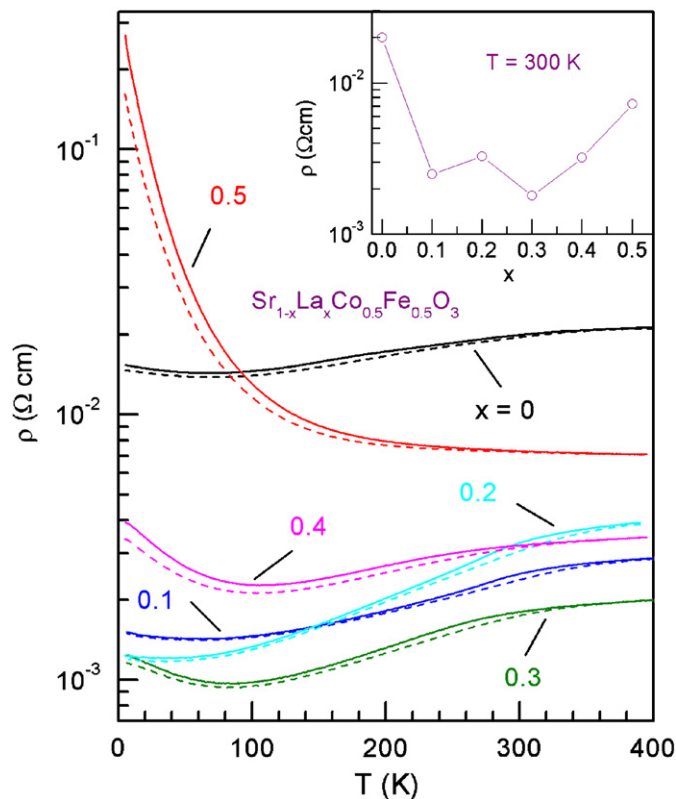

Fig. 7. Temperature dependence of electrical resistivity for Sr$_{1-x}$La$_x$Co$_{0.5}$Fe$_{0.5}$O$_3$. Solid lines represent the resistivity in a zero magnetic field. Dashed lines denote the resistivity in a magnetic field of 70 kOe. Inset shows the zero-field resistivity at $T = 300$ K.

around $x = 0.1$–0.2. The observed oxygen deficiency may result in the lowering of T_C for $x < 0.2$.

Temperature dependence of electrical resistivity for Sr$_{1-x}$La$_x$Co$_{0.5}$Fe$_{0.5}$O$_3$ is presented in Fig. 7, in a zero magnetic field an in a magnetic field of 70 kOe. The undoped material shows metallic resistivity with a slight upturn below $\sim$70 K. On La substitution, the resistivity initially decreases and then increases with a stronger tendency to become more insulating/semiconductive at low temperatures. The inset to Fig. 7 demonstrates this tendency for the resistivity at $T = 300$ K. For all samples except the nonmetallic $x = 0.5$ a small decrease of resistivity below T_C is observed denoting decreased electron spin scattering. For a low-La substitution, a slight magnetoresistance is observed just below T_C. This behavior is characteristic of those ferromagnetic oxides, including manganites, ruthenates, and cobaltites, for which resistivity is metallic above and below T_C. The increase of La substitution results in a moderately increased magnetoresistance at lower temperatures, which may be a grain boundary effect.

5. Summary

We have obtained an oxygen-vacancy-ordered Sr$_8$Co$_4$Fe$_4$O$_{23}$ compound and nearly oxygen stoichiometric Sr$_{1-x}$La$_x$Co$_{0.5}$Fe$_{0.5}$O$_3$ ($0.1 \leqslant x \leqslant 0.5$) samples by means of solid state synthesis and annealing under moderately high oxygen pressures. Analysis of the room temperature neutron diffraction data reveal that the SrCo$_{0.5}$Fe$_{0.5}$O$_{2.89}$ sample exhibits $I4/mmm$ symmetry and is similar to the formerly reported, oxygen-vacancy-ordered Sr$_8$Fe$_8$O$_{23}$ compound [15]. Structural analysis of the NPD data clearly shows that such an analysis must be performed carefully, as the ordering of the oxygen sublattice may manifest itself in a form of very weak

Fig. 6. Dependence of M_{sat}, μ_{eff} (top) and T_c and Θ (bottom) with La content. The dashed line shows the model for the dependence of M_{sat}, described in the text. The solid lines denote two models for $\mu_{eff}(x)$ with different spin states for Co$^{4+/3+}$: high-spin, HS and intermediate-spin, IS.

peaks, not visible in the X-ray diffraction. At room temperature, we have identified cubic symmetry $Pm\bar{3}m$ for samples with $x = 0.1$ and 0.2, tetragonal $I4/mcm$ symmetry for samples with $x = 0.3$ and 0.4 and monoclinic $I12/c1$ symmetry for $Sr_{0.5}La_{0.5}Co_{0.5}Fe_{0.5}O_3$ compound. Rietveld analysis of NPD data shows that substitution of larger Sr^{2+} by smaller La^{3+} is accompanied by an even larger increase of the average B-site ion size, as observed from the Fe/Co–O bond distances, the tolerance factor, and the lowering of the symmetry with increasing x. The phase transition to an orthorhombic $Ibam$ structure observed for $Sr_{0.6}La_{0.4}Co_{0.5}Fe_{0.5}O_{3.00(1)}$ at low temperatures is not related to the change in the tilt mode of the octahedra, but by the differentiation of the Fe/Co–O equatorial bond distances indicating a change in the electronic structure with temperature.

Low-temperature structural and magnetic measurements show a ferromagnetic ordering with the maximum Curie temperature near 290 K at $x = 0.2$. Magnetization measurements revealed a sharp decrease of T_C for the samples with $x > 0.3$ that well correlates with the development of a more rapid distortion of the structure. It seems that to describe the observed nonlinear behavior of structural parameters and T_C a nonlinear decrease of the oxidation state of Co and Fe as well as a possible increase of Co spin state should be invoked.

Acknowledgments

References

[1] Y. Teraoka, H.-M. Zhang, N. Yamazoe, Chem. Lett. (1985) 1743–1746.
[2] Y. Teraoka, T. Nobunaga, N. Yamazoe, Chem. Lett. (1988) 503–506.
[3] H. Kruidhof, H.J.M. Bouwmeester, R.H.E.v. Doorn, A.J. Burggraaf, Solid State Ionics 63–65 (1993) 816–822.
[4] L. Qiu, T.H. Lee, L.-M. Liu, Y.L. Yang, A.J. Jacobson, Solid State Ionics 76 (1995) 321–329.
[5] J.W. Stevenson, T.R. Armstrong, R.D. Carneim, L.R. Pederson, W.J. Weber, J. Electrochem. Soc. 143 (9) (1996) 2722–2729.
[6] S. Li, W. Jin, N. Xu, J. Shi, Solid State Ionics 124 (1999) 161–170.
[7] Y. Teraoka, Y. Honbe, J. Ishii, H. Furukawa, I. Moriguchi, Solid State Ionics 152–153 (2002) 681–687.
[8] Y. Teraoka, H.-M. Zhang, K. Okamoto, N. Yamazoe, Mater. Res. Bull. 23 (1988) 51–58.
[9] A. Petric, P. Huang, F. Tietz, Solid State Ionics 135 (2000) 719–725.
[10] E. Maguire, B. Gharbage, F.M.B. Marques, J.A. Labrincha, Solid State Ionics 127 (2000) 329–335.
[11] A. Esquirol, N.P. Brandon, J.A. Kilner, M. Mogensen, J. Electrochem. Soc. 151 (2004) A1847–A1855.
[12] P.K. Gallaher, J.B. MacChesney, D.N.E. Buchanan, J. Chem. Phys. 41 (1964) 2429–2434.
[13] P.D. Battle, T.C. Gibb, P. Lightfoot, J. Solid State Chem. 76 (1988) 334–339.
[14] O.H. Hansteen, H. Fjellvag, B.C. Hauback, J. Solid State Chem. 141 (2) (1998) 411–417.
[15] J.P. Hodges, S. Short, J.D. Jorgensen, X. Xiong, B. Dabrowski, S.M. Mini, C.W. Kimball, J. Solid State Chem. 151 (2000) 190–209.
[16] W.T.A. Harrison, T.H. Lee, Y.L. Yang, D.P. Scarfe, L.M. Liu, A.J. Jacobson, Mater. Res. Bull. 30 (5) (1995) 621–630.
[17] L.M. Liu, T.H. Lee, L. Qiu, Y.L. Yang, A.J. Jacobson, Mater. Res. Bull. 31 (1) (1996) 29–35.
[18] L.V. Kokhanovskii, V.V. Vashuk, O.P. Ol'shevskaya, O.I. Kirilenko, Inorg. Mater. 37 (7) (2001) 730–736.
[19] S. Kolesnik, B. Dabrowski, J. Mais, D.E. Brown, R. Feng, O. Chmaissem, R. Kruk, C.W. Kimball, Phys. Rev. B 67 (14) (2003) 144402.
[20] B. Dabrowski, unpublished.
[21] D. Mantzavinos, A. Hartley, I.S. Metcalfe, M. Sahibzada, Solid State Ionics 134 (2000) 103–109.
[22] V.A. Cherepanov, L.Ya. Gavrilova, T.V. Aksenova, M.V. Ananyev, E. Bucher, G. Caraman, W. Sitte, V.I. Voronin, Prog. Solid State Chem. 35 (2007) 175–182.
[23] M. Katsuki, S. Wang, M. Dokiya, T. Hashimoto, Solid State Ionics 156 (2003) 453–461.
[24] S. McIntosh, J.F. Vente, W.G. Haije, D.H.A. Blank, H.J. Bouwmeester, Solid State Ionics 177 (2006) 833–842.
[25] Y. Takeda, R. Kanno, T. Takada, O. Yamamoto, M. Takano, Y. Bando, Z. Anorg. Allg. Chem. 540 (9–10) (1986) 259–270.
[26] S. Kawasaki, M. Takano, Y. Takeda, J. Solid State Chem. 121 (1996) 174–180.
[27] R. Le Toquin, W. Paulus, A. Cousson, C. Prestipino, C. Lamberti, J. Am. Chem. Soc. 128 (40) (2006) 13161–13174.
[28] P. Bezdicka, A. Wattiaux, J.C. Grenier, M. Pouchard, P. Hagenmuller, Z. Anorg. Allg. Chem. 619 (1993) 7–12.
[29] P. Bezdicka, L. Fournès, A. Wattiaux, J.C. Grenier, M. Pouchard, Solid State Commun. 91 (7) (1994) 501–505.
[30] S. Balamurugan, K. Yamaura, A.B. Karki, D.P. Young, M. Arai, E. Takayama-Muromachi, Phys. Rev. B 74 (2006) 172406.
[31] J. Marzec, J. Power Sources 173 (2007) 671–674.
[32] A. Muñoz, J.A. Alonso, M.J. Martínez-Lope, C. de la Calle, M.T. Fernández-Díaz, J. Solid State Chem. 179 (2006) 3365–3370.
[33] M. Imada, A. Fujimori, Y. Tokura, Rev. Mod. Phys. 70 (4) (1998) 1039–1263.
[34] R. Sonntag, S. Neov, V. Kozhukharov, D. Neov, J.E. ten Elshof, Physica B 241-243 (1998) 393–396.
[35] V.G. Sathe, S.K. Paranjpe, V. Siruguri, A.V. Pimpale, J. Phys.: Condens. Matter 10 (1998) 4045–4055.
[36] D.V. Karpinsky, I.O. Troyanchuk, V.M. Dobryansky, R. Szymczak, M. Tovar, Crystallogr. Rep. 51 (4) (2006) 596–600.
[37] N.V. Khiem, L.V. Bau, N.M. An, N.X. Phuc, D.N.H. Nam, Physica B 327 (2003) 187–189.
[38] T. Takeda, Y. Yamaguchi, H. Watanabe, J. Phys. Soc. Jpn. 33 (4) (1972) 967–969.
[39] J.B. MacChesney, R.C. Sherwood, J.F. Potter, J. Chem. Phys. 43 (6) (1965) 1907–1913.
[40] T. Takeda, S. Komura, H. Fujii, J. Magn. Magn. Mater. 31–34 (1983) 797–798.
[41] M. Takano, J. Kawachi, N. Nakanishi, Y. Takeda, J. Solid State Chem. 39 (1) (1981) 75–84.
[42] A.E. Bocquet, A. Fujimori, T. Mizokawa, T. Saitoh, H. Nagatame, S. Suga, N. Kimizuka, Y. Takeda, M. Takano, Phys. Rev. B 45 (4) (1992) 1561–1570.
[43] H. Adachi, M. Takano, J. Solid State Chem. 93 (2) (1981) 556–566.
[44] S. Mathi Yada, R. Jagadish, R.S. Rao, R. Asokamani, Phys. Rev. B 43 (16) (1991) 13274–13279.
[45] H. Taguchi, M. Shimada, M. Koizumi, Mater. Res. Bull. 15 (2) (1980) 165–169.
[46] H. Taguchi, M. Shimada, M. Koizumi, J. Solid State Chem. 29 (2) (1979) 221–225.
[47] H. Taguchi, M. Shimada, M. Koizumi, Mater. Res. Bull. 13 (11) (1978) 1225–1230.
[48] R.H. Potze, G.A. Sawatzky, M. Abbate, Phys. Rev. B 51 (17) (1995) 11501–11506.
[49] M. Zhuang, W. Zhang, A. Hu, N. Ming, Phys. Rev. B 57 (21) (1998) 13655–13659.
[50] M. Abbate, G. Zampieri, J. Okamoto, A. Fujimori, S. Kawasaki, M. Takamoto, Phys. Rev. B 65 (21) (2002) 165120.
[51] A. Maignan, C. Martin, N. Nguyen, B. Raveau, Solid State Sci. 3 (1–2) (2001) 57–63.
[52] B. Raveau, V. Pralong, V. Caignaert, M. Hervieu, A. Maignan, J. Phys.: Condens. Matter 17 (46) (2005) 7371–7382.
[53] J.D. Jorgensen, J. Faber Jr., J.M. Carpenter, R.K. Crawford, J.R. Haumann, R.L. Hitterman, R. Kleb, G.E. Ostrowski, F.J. Rotella, T.G. Worlton, J. Appl. Cryst. 22 (1989) 321–333.
[54] A.C. Larson, R.B. Von Dreele, Los Alamos Natl. Lab. Rep.—LAUR (2004) 86–748.
[55] B.H. Toby, J. Appl. Cryst. 34 (2001) 210–221.
[56] B. Dabrowski, O. Chmaissem, J. Mais, S. Kolesnik, J.D. Jorgensen, S. Short, J. Solid State Chem. 170 (1) (2003) 154–164.
[57] A.M. Glazer, Acta Cryst. B 28 (11) (1972) 3384–3392.